ARTICLES
https://doi.org/10.1038/s41566-019-0367-9

nature photonics

Transverse localization of transmission eigenchannels

Hasan Yılmaz [1], Chia Wei Hsu [1], Alexey Yamilov [2] and Hui Cao [1*]

Transmission eigenchannels are building blocks of coherent wave transport in diffusive media, and selective excitation of individual eigenchannels can lead to diverse transport behaviour. An essential yet poorly understood property is the transverse spatial profile of each eigenchannel, which is relevant for the associated energy density and critical for coupling light into and out of it. Here, we discover that the transmission eigenchannels of a disordered slab possess exponentially localized incident and outgoing profiles, even in the diffusive regime far from Anderson localization. Such transverse localization arises from a combination of reciprocity, local coupling of spatial modes and non-local correlations of scattered waves. Experimentally, we observe signatures of such localization even with finite illumination area. The transverse localization of high-transmission channels enhances optical energy densities inside turbid media, which will be important for light–matter interactions and imaging applications.

Spatial inhomogeneities in the refractive index of a disordered medium cause multiple-scattering of light. In disordered media such as biological tissue, white paint and clouds, most of the incident light reflects back, hindering the transfer of energy and information through the media. However, by utilizing the interference of scattered waves, it is possible to prepare optimized wavefronts that completely suppress reflection—a striking phenomenon first predicted in the context of mesoscopic electron transport[1–4]. The required incident wavefronts are the eigenvectors of $t^{\dagger}t$ where t is the field transmission matrix; the corresponding eigenvalues give the total transmission. In a lossless diffusive medium, the transmission eigenvalues τ span from 0 to 1, leading to closed ($\tau \approx 0$) and open ($\tau \approx 1$) channels. In recent years, spatial light modulators (SLMs) have been used to excite the open channels[5–14] to enhance light transmission through diffusive media. Selective excitation of individual channels can dramatically change the total energy stored inside the random media as well as the spatial distribution of energy density[14–20].

Some important questions regarding the transmission eigenchannels remain open. What are the transverse spatial profiles for coupling light into such channels? Once coupled in, how do the eigenchannels spread in the transverse direction? In the Anderson localization regime of transport, a high-transmission channel is formed by coupled spatially localized modes[21–26], so transversely localized excitation and propagation are expected. However, Anderson localization is extremely hard to achieve in three-dimensional (3D) disordered systems[27], and diffusive transport is much more common. In the diffusive regime, the open channels are expected to cover the entire transverse extent of the system[15,24], utilizing all available spatial degrees of freedom.

Here, we discover that the transmission eigenchannels are transversely localized even in the diffusive regime of transport. In a disordered slab of width W much larger than thickness L, all transmission eigenchannels have a finite transverse extent that is much smaller than W. In the $W \to \infty$ limit, the channel width approaches an asymptotic value D_{∞}, which scales as $(kl_t)L$ in two dimensions. Here l_t is the transport mean free path and k the effective wavenumber in the slab. Moreover, all eigenchannels feature an exponential decay in their transverse intensity profiles, and they do not spread laterally while propagating through the slab. These properties can be explained in terms of optical reciprocity, the bandedness of the real-space transmission matrix and non-local correlations of multiply scattered waves. The transverse eigenchannel localization in the diffusive regime is a distinct physical phenomenon from the previously known transverse localization in Anderson-localized systems[28–33]. Experimentally, we observe that high-transmission channels are exponentially localized in the transverse directions on both front and back surfaces of a diffusive slab made of ZnO nanoparticles. For finite-area illumination, the transverse extent of a high-transmission channel is smaller than the illumination area, and its lateral spreading in the diffusive slab is suppressed. The transverse localization of high-transmission channels greatly enhances the energy densities of both transmitted light and light inside the slab. It therefore has a potential impact on the advancements of deep-tissue imaging, optogenetics[34–36] and the manipulation of light–matter interactions inside turbid media[37,38].

Transverse localization of eigenchannels

To achieve complete characterization of the transmission eigenchannels we performed numerical simulations where we can exert full control over the incident wavefront and systematically explore the entire parameter space of interest. We first calculated the field transmission matrix t of a 2D diffusive slab using the recursive Green's function method[39], then computed the spatial profiles of individual eigenchannels (see Methods). Remarkably, in wide slabs, we observe that the eigenchannels are exponentially localized in the transverse direction parallel to the slab (an exemplary open channel is shown in Fig. 1a). Even though we impose no constraint on where or how wide the incident wavefront should be, the resulting eigenchannel only occupies a relatively small transverse extent, utilizing just a fraction of the spatial degrees of freedom that are available across the width of the structure. Moreover, the eigenchannel does not spread laterally as it propagates through the disordered slab; the transmitted profile is also localized, with a width similar to that of

[1]Department of Applied Physics, Yale University, New Haven, CT, USA. [2]Department of Physics, Missouri University of Science & Technology, Rolla, MO, USA. *e-mail: hui.cao@yale.edu

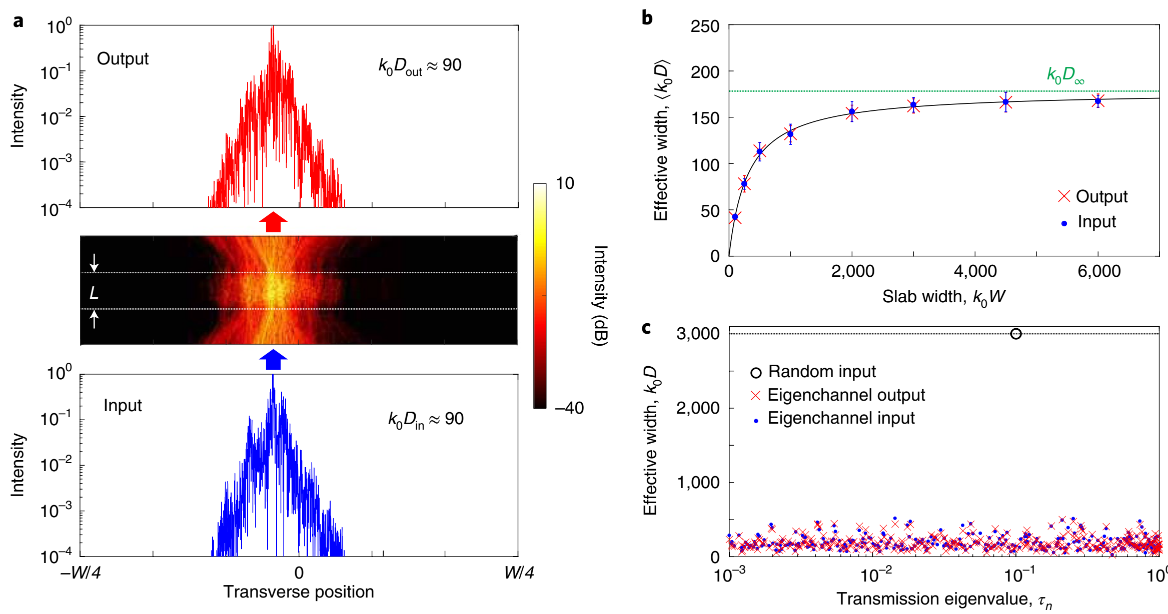

Fig. 1 | Transverse localization of transmission eigenchannels. Numerical results of 2D diffusive slabs with normalized thickness $k_0L=50$, transport mean free path $n_0k_0l_t=4.6$, effective refractive index $n_0=1.5$ and average transmission eigenvalue $\langle\tau\rangle=0.10$. $k_0=2\pi/\lambda$, where λ is the vacuum wavelength. **a**, Intensity profile of the highest-transmission eigenchannel ($\tau_1=0.9999$) in a slab of normalized width $k_0W=6{,}000$, revealing localization in the transverse direction. White dashed lines in the middle panel indicate the surfaces of the slab, and the relative vertical to horizontal scale is set to 5:1. The log-linear plots of the incident and transmitted intensity profiles on the input and output surfaces of the slab (lower and upper panels) reveal exponential decay in the transverse direction. **b**, Average input and output widths $\langle D_{in}\rangle$ and $\langle D_{out}\rangle$ of open channels ($\tau_n\geq 1/e$) versus slab width k_0W. They are equal and approach an asymptotic value D_∞ (green dashed line) in the wide-slab limit due to transverse localization. Each data point is an average over 10 realizations of structural disorder, and the error bars give the standard deviation among realizations. The black solid line is the fitting that gives D_∞ in the $W\to\infty$ limit. **c**, Eigenchannel widths versus transmission eigenvalues τ_n for $k_0W=6{,}000$, revealing that all eigenchannels are transversely localized with no lateral spreading from input to output.

the incidence. As shown in the log-linear plot in Fig. 1a, the transverse profile decays exponentially on both input and output surfaces, which is surprising given that the wave transport is diffusive.

A legitimate question is whether such transverse localization of eigenchannels persists in large systems, as experimentally the slab width W is typically so large that it can be regarded as infinite. To find the answer, we carry out a scaling analysis with increasing W. We quantify the width of an eigenchannel via the definition of the participation number (see Methods). As shown in Fig. 1b, input and output channel widths D_{in} and D_{out} are identical after ensemble averaging. In the $W\to\infty$ limit of interest, the open channel remains transversely localized, and its width saturates to an asymptotic value that we denote D_∞. The extrapolation of D_∞ in the $W\to\infty$ limit is described in Supplementary Section 2.4.

The absence of eigenchannel spreading, $\langle D_{in}\rangle=\langle D_{out}\rangle$, can be explained by reciprocity. Lorentz reciprocity requires the scattering matrix to be symmetric[40], so the transmission matrix coming from one side must be the transpose of the transmission matrix coming from the other side. Singular value decomposition of the transmission matrix gives $t=U\sqrt{\tau}V^\dagger$, where the nth columns of V and U are the normalized input and output wavefronts of the nth eigenchannel with transmission eigenvalue τ_n. Since $t^{\mathrm{T}}=V^*\sqrt{\tau}(U^*)^\dagger$, reciprocity demands that the phase conjugation of the nth eigenchannel output must be precisely the input of the nth eigenchannel incident from the other side, with the same eigenvalue. If the disordered medium is statistically equivalent for light incident from either side, the eigenchannel input width must be statistically identical for both directions. Thus the input and output channel widths should be the same after ensemble averaging.

The above argument applies to all eigenchannels, open or closed. Our numerical simulations confirm that all transmission eigenchannels are transversely localized with no lateral spreading, as shown in Fig. 1c. In this example, the widths of all eigenchannels are one order of magnitude smaller than the slab width. The channel width D fluctuates around the mean $\langle D\rangle$ (a histogram of $D/\langle D\rangle$ is presented in Supplementary Fig. 7).

By defining the centre position of an eigenchannel via the centre of mass of its lateral intensity profile, we find that the eigenchannels are randomly and uniformly distributed over the entire width of the slab (Supplementary Fig. 5). An exponential fitting of the tails of their intensity profiles confirms that all eigenchannels decay exponentially in the transverse direction. The decay length is proportional to the channel width, as shown in Supplementary Fig. 7.

Origin of transverse localization

While reciprocity explains the absence of lateral spreading, it remains to be answered why the eigenchannels are transversely localized in the first place. We can gain insight by examining the real-space transmission matrix. Although scattering ensures that light with a specific incident angle is coupled into all outgoing angles once the slab thickness L exceeds the transport mean free path l_t, this is not the case in real space. Given a point-like excitation at the input surface, light spreads laterally as it diffuses through the disordered slab, covering a finite extent of width on the order of L at the output surface (this is shown in Fig. 2a). Such geometric local spreading is the origin of the much celebrated 'memory effect'[41–44]. As a result, the input and output spatial modes are not fully mixed, which emerge as non-vanishing elements only within a distance of $\sim L$ to the diagonal of the real-space transmission matrix (that is, the surface-to-surface Green's function), as shown in Fig. 2b. It is noteworthy that 2D Anderson localization is absent in our systems, because the real-space transmission matrix bandwidth is

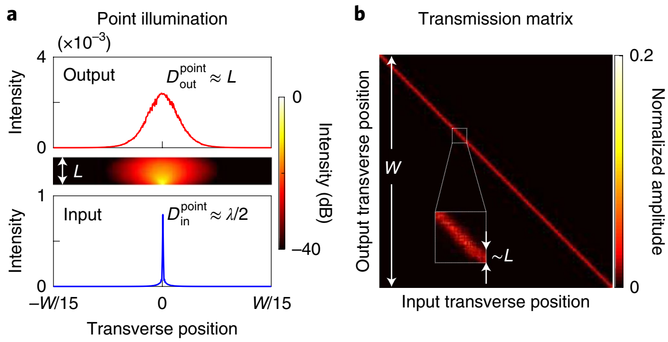

Fig. 2 | Bandedness of the real-space transmission matrix. a, Calculated intensity profile inside a disordered slab when the incident light is focused to a diffraction-limited spot at the front surface, showing the extent of transverse spreading as light diffuses through the slab. D_{in}^{point} and D_{out}^{point} are the beam widths at the input and output surfaces. The intensity profiles shown are ensemble averaged over 1,000 realizations of disorder. **b**, Amplitudes of complex elements of the real-space transmission matrix. While the matrix size is given by the slab width W, only elements within a distance ~L from the diagonal are non-vanishing, because the extent of diffusive spreading in the slab is much less than the slab width. The simulation parameters are the same as in Fig. 1a. Inset: expanded view of a part of the matrix.

proportional to the sample thickness in all of the systems we study here (Supplementary Fig. 4). Similarly, the real-space matrix $t^\dagger t$ also exhibits a bandwidth proportional to L.

Random matrices with dominant near-diagonal elements were previously studied in the context of quantum chaos, and it was found that the eigenvectors of such 'banded random matrices' are exponentially localized[45–47]. It is therefore tempting to explain the transverse localization of eigenchannels through the 'bandedness' of real-space transmission matrix for a wide slab. The standard theory of banded random matrices predicts that when the elements of a Hermitian random matrix are non-vanishing within a band of size b, the eigenvectors are localized with participation numbers proportional to b^2 (refs. [45–47]). In the present context, one would then expect the normalized eigenchannel width kD to be on the order of $(kL)^2$ because the dimensionless bandwidth is $b \approx kL$. For the example in Fig. 1, this argument suggests $kD_\infty \approx 5{,}600$, as confirmed numerically in Supplementary Fig. 8, but the actual eigenchannel width is only 90. The far smaller channel width indicates a much stronger transverse localization, which is beyond the standard banded random matrix theory.

To explore what determines the asymptotic open channel width D_∞, we carried out a systematic study to map out its dependence on the slab thickness L and the transport mean free path l_t. As shown in Fig. 3a, the open channel width D_∞ scales linearly with the slab thickness L that determines the real-space transmission matrix bandwidth b, in contrast to predictions from the standard banded random matrix theory. Meanwhile, even though l_t does not affect the real-space transmission matrix bandwidth b, we find in Fig. 3b that the open channel width D_∞ also scales linearly with l_t. A dimensional analysis and the scale invariance of the electromagnetic wave equation indicates a prefactor proportional to the wavenumber $k = n_0 k_0$. Putting these together, we expect a scaling of $D_\infty \propto (kl_t)L$. In Fig. 3c we plot the compiled data of D_∞ as a function of $(kl_t)L$ from $6\times6=36$ combinations of (L,l_t) for $n_0 = 1.5$ and $6\times2=12$ combinations of (L,l_t) for $n_0=1$; each D_∞ is extrapolated from 8 widths of W and 10 realizations of disorder (totalling >3,000 configurations). Indeed, we observe the $D_\infty \propto (kl_t)L$ scaling. A least-squares fit determines the proportionality constant to be 0.68, close to 2/3. Note that previous studies[15,24] did not find such transverse localization in the diffusive transport regime because the system width W in the previous simulations was not wide enough. Also, note that such eigenchannel width D_∞ is generally far smaller than the 2D localization length $\xi_{2D} \approx l_t e^{\pi k l_t/2}$.

The reduction in eigenchannel width from kL^2 to kl_tL requires explanations beyond the bandedness of the real-space transmission matrix. The key factor is the correlations among the non-zero matrix elements induced by multiple scattering of light inside the slab, which are referred to as non-local correlations[48–60]. Stronger scattering (smaller kl_t) enhances non-local correlations and leads to tighter transverse localization. When we replace the non-vanishing elements of the real-space transmission matrix with uncorrelated complex Gaussian random numbers, we observe much wider eigenchannel widths that scale as kL^2, as predicted by standard banded random matrix theory (Supplementary Fig. 8).

Extending such scaling study to disordered slabs in 3D is a daunting computational task. Nevertheless, we expect transverse localization of transmission eigenchannels in 3D diffusive systems, because such systems also possess banded real-space transmission matrices, non-local correlations and reciprocity.

Experiments with finite-area illumination

In practical applications, finite-area illumination is commonly used. Accordingly, in this and the next sections we investigate the effects of transverse localization when the size of an illumination beam is smaller than the asymptotic channel width D_∞. Experimentally, we measure the spatial profiles of individual eigenchannels at the input and output surfaces of a 3D scattering slab. The sample consists of ZnO nanoparticles that are spin-coated on a cover slide. The thickness of the ZnO layer is about 10 μm, much less than the lateral dimension of the layer (2 cm × 2 cm). The average transmittance of light at a wavelength of 532 nm is approximately 0.2.

We start by measuring the transmission matrix of the disordered slab. A simplified schematic of the experimental set-up is shown in Fig. 4a, with a detailed one given in Supplementary Fig. 1. A spatially uniform monochromatic laser beam at wavelength $\lambda = 532$ nm is modulated by a phase-only SLM. The SLM surface is imaged by a pair of lenses onto the pupil of a microscope objective. The spatial profile of illumination is thus the 2D Fourier transform of the SLM phase pattern. The illumination area is finite, and its width scales inversely with the SLM macropixel size. We use the SLM and a camera (CCD2) to measure the field transmission matrix in k-space, with a common-path interferometry method akin to refs. [13,61]. The number of SLM macro-pixels that modulate the input beam is 2,048, and the number of output speckle grains recorded by the camera is about 15,000.

After measuring the field transmission matrix t, we determine the incident wavefronts of individual eigenchannels from the eigenvectors of $t^\dagger t$. Then we display the corresponding phase patterns on the SLM, and record the 2D spatial intensity profiles $I(x,y)$ that are incident on the front surface and transmitted to the back surface of the sample with two cameras (CCD1, CCD3). We define the effective area of such a profile by the 2D participation number A (see Methods) and the effective width $D = 2\sqrt{A/\pi}$.

A random wavefront exhibits an effective width of $D_{in}^{rand} \approx 13$ μm and $D_{out}^{rand} \approx 21$ μm on two sides of the slab (shown in Fig. 4b,c). In contrast, the highest-transmission eigenchannel has narrower spatial profiles at both input and output (Fig. 4d,e): $D_{in}^{high} \approx 10$ μm and $D_{out}^{high} \approx 14$ μm. Its lateral spreading is also less: $\Delta D^{high} = D_{out}^{high} - D_{in}^{high} \approx 4$ μm, in contrast to $\Delta D^{rand} \approx 8$ μm ~ L for random wavefronts. The enhanced lateral confinement and suppressed spreading lead to a significant increase in the energy density inside the slab. On the back surface, the energy density, averaged over the cross-section of the transmitted beam, is enhanced $\left(T^{high}(D_{in}^{rand})^2\right)/\left(\langle T\rangle (D_{in}^{high})^2\right) = 4.4$ times, which is more than twice the enhancement of total transmitted power $T^{high}/\langle T\rangle = 1.95$.

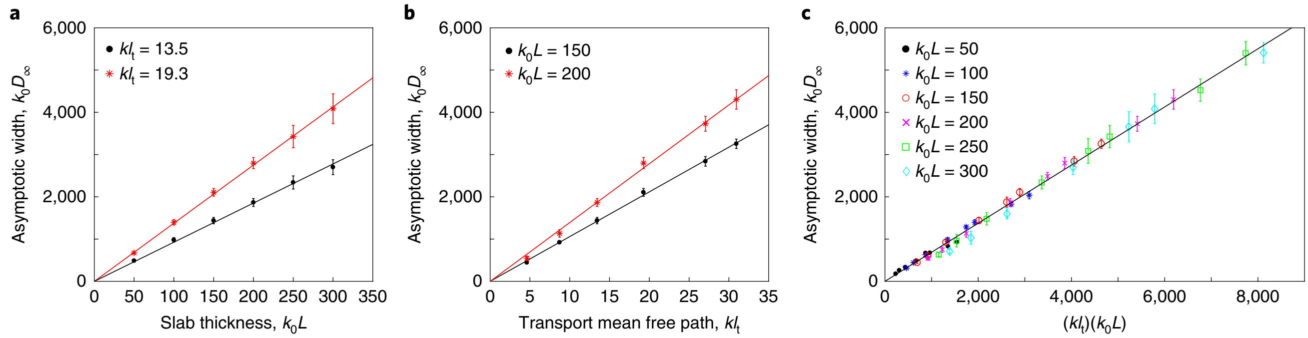

Fig. 3 | Scaling of the asymptotic channel width in diffusive slabs. a, Asymptotic width D_∞ of open channels as a function of slab thickness L when the transport mean free path l_t is fixed. The solid lines represent a linear fit. The slope is smaller when l_t is shorter. **b**, D_∞ as a function of l_t for fixed L. The solid lines are a linear fit, and the slope increases with L. **c**, D_∞ for diffusive slabs of different L, l_t and n_0, showing a general scaling $D_\infty \propto (n_0k_0l_t)L$. Linear regression gives a proportionality constant of 0.68 (black solid line). Each data point represents an ensemble average over all open channels (with $\tau_n \geq 1/e$) in 10 realizations of disorder. Error bars are the standard deviation among the realizations.

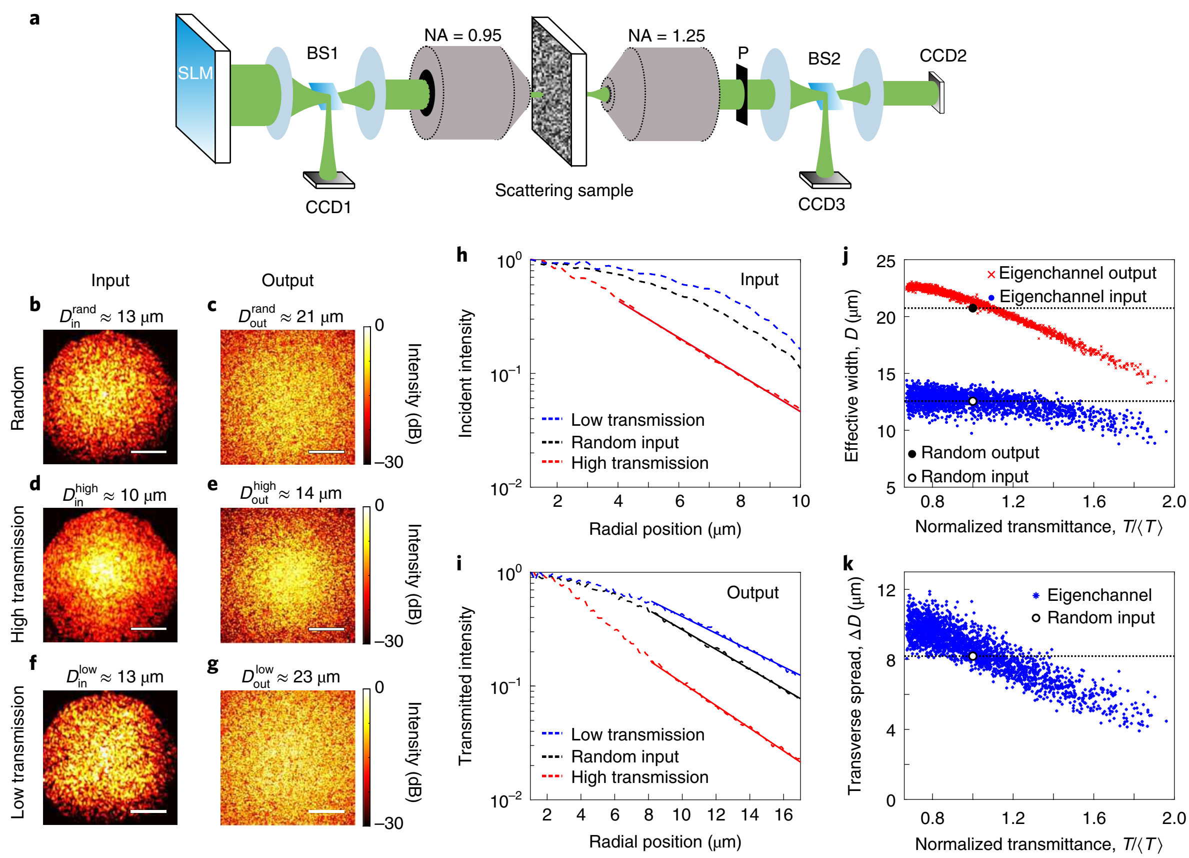

Fig. 4 | Experimental signatures of transverse localization for high-transmission channels. a, Simplified schematic of the experimental set-up for measuring the field transmission matrix of a 3D disordered slab with a finite illumination area, followed by selective excitation of individual transmission eigenchannels and measurement of their incident and transmitted intensity profiles on the front and back surfaces of the sample. BS, beamsplitter; CCD, charge-coupled device camera; NA, numerical aperture; P, linear polarizer. **b–g**, Intensity profiles of a random incident wavefront (**b**,**c**), a high-transmission channel (**d**,**e**) and a low-transmission channel (**f**,**g**) on the front (**b**,**d**,**f**) and back (**c**,**e**,**g**) surfaces of the sample. Scale bars, 6 μm. **h**,**i**, Normalized radial intensity profiles of random incident wavefront (black), high-transmission (red) and low-transmission (blue) channels on the front (**h**) and the back (**i**) surfaces of the sample. Dashed lines are measured intensities averaged azimuthally and over 20 random wavefronts or 20 high/low transmission channels. Solid lines are exponential fits to the tails, with decay lengths of 2.6 μm (high-transmission input), 4 μm (high-transmission output), 5 μm (random output) and 6 μm (low-transmission output), respectively. Only high-transmission channels exhibit exponential decay at input. **j**, Input width (blue filled circles) and output width (red crosses) of all 2,048 eigenchannels as a function of the normalized transmittance $T/\langle T \rangle$. Dashed lines denote the input width (black open circle) and output width (black filled circle) for random incident wavefronts. **k**, Transverse spreading $\Delta D = D_{out} - D_{in}$ versus the normalized transmittance $T/\langle T \rangle$ for experimentally measured transmission eigenchannels.

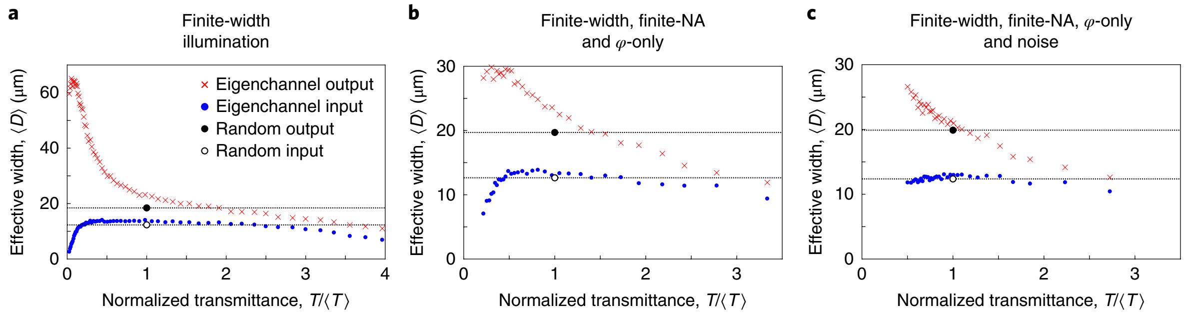

Fig. 5 | Modification of transmission eigenchannel widths by incomplete control. **a**, Numerically calculated input width (blue circles) and output width (red crosses) of all transmission eigenchannels as a function of the normalized transmittance in 2D diffusive slabs with local illumination. Each data point represents an ensemble average over 50 realizations of disorder. For a random wavefront, the incident beam width at the front surface of the slab is $D_{in}^{rand} \approx 13\,\mu m$ (black open circle), and the transmitted beam width at the back surface is $D_{out}^{rand} \approx 19\,\mu m$ (filled black circle). **b**, Including finite NA for illumination and detection, as well as phase-only (φ-only) modulation of the incident wavefront, reduces the range of eigenchannel widths. **c**, Adding random Gaussian noise to the transmission matrix further modifies the eigenchannel widths, especially for the low-transmission channels. The slab width is $W = 508\,\mu m$, the thickness is $L = 10\,\mu m$, the transport mean free path is $l_t = 1\,\mu m$ and the average refractive index is $n_0 = 1.4$. The slab is sandwiched between air (refractive index $n_1 = 1.0$) and glass (refractive index $n_2 = 1.5$). The calculated input and output intensity profiles for high- and low-transmission eigenchannels in Supplementary Fig. 9 agree well with the experimental data in Fig. 4h,i.

More complex behaviours emerge when we examine eigenchannels with lower transmittance. In our experiment, the low-transmission eigenchannels have incident profiles (Fig. 4f) comparable in size to those of random wavefronts, but with enhanced lateral spreading that leads to wider output profiles (Fig. 4g).

For a more detailed look at the spatial profiles, in Fig. 4h,i we plot the radial intensity profiles for random wavefronts, high-transmission and low-transmission channels at the input and output surfaces, after azimuthal averaging and ensemble averaging. The random wavefronts exhibit sinc^2 profiles on the front surface (see Supplementary Fig. 2 for more details) and have an exponentially decaying tail with $5\,\mu m$ decay length at the back surface due to diffusion. In comparison, the high-transmission channels have exponentially decaying tails on both front and back surfaces, with a decay length of $2.6\,\mu m$ at the front and $4\,\mu m$ at the back. The exponential decay on the front surface and the enhanced decay rate on the back surface, as well as the transverse confinement ($D_{in}^{high} < D_{in}^{rand}$) and the suppressed lateral spreading ($\Delta D^{high} < \Delta D^{rand}$), are signatures of transverse localization of high-transmission channels[62,63].

Figure 4j shows the input and output widths of all of the 2,048 eigenchannels as a function of the normalized transmittance, and compares them to random incident wavefronts. In contrast to Fig. 1c, the eigenchannel widths reveal systematic dependences on the transmittance, particularly for D_{out}. Figure 4k shows that the transverse spreading increases with decreasing transmittance, with the high-transmission eigenchannels exhibiting suppressed lateral spreading and the low-transmission eigenchannels enhanced spreading. In the next section, we show that these properties are also observed numerically when finite illumination area, phase-only modulation, and measurement noises are taken into account in the simulations.

Effect of incomplete control

There are important differences between the experimental set-up and the ideal scenario considered in Figs. 1 and 3. In our experiment, the illumination beam width on the sample surface is comparable to L. Also, we use phase-only modulation over a fraction of incident angles, and collect a fraction of outgoing angles in one polarization. Such experimental conditions lead to incomplete control, which is known to affect the transmittance of eigenchannels[13,64], and we expect them to also modify the eigenchannel profiles. Experimentally it is not possible to separate the different factors, but we can do so with simulations. Numerically we consider 2D disordered slabs with parameters comparable to the experiment (see the caption of Fig. 5), and the asymptotic open-channel width is $D_\infty \approx 90\,\mu m$. Naturally we do not expect quantitative comparison with the 3D sample in the experiment, but we aim to gain physical insights that do not depend on dimensionality.

We describe finite-width illumination by grouping incident modes into equally spaced intervals of transverse momenta that model the SLM macropixels[13]. For random incident wavefronts, the beam widths as defined by the participation number are $D_{in}^{rand} \approx 13\,\mu m$ on the front and $D_{out}^{rand} \approx 19\,\mu m$ on the back surface. Despite the illumination beam width D_{in}^{rand} being much smaller than the asymptotic eigenchannel width D_∞, both high-transmission and low-transmission channels have input widths even smaller than D_{in}^{rand} (Fig. 5a). We attribute this to the fact that these channels utilize multipath interference to enhance or suppress the transmittance. Indeed, crossings of scattering paths inside the sample lead to non-local correlations[52,60] and enhance the range of transmission eigenvalues[13]. Therefore, eigenchannels with extremal eigenvalues prefer smaller input beam widths to increase the probability of crossing. In addition, the extremal eigenchannels preferentially enhance or suppress the intensity near the centre of the transmitted beam (Supplementary Fig. 11). Such a non-uniform modification of the transmitted intensity profile results in an effective reduction of the participation number D_{out} for the high-transmission eigenchannels that we observe in Fig. 5a, and similarly for the increased D_{out} of the low-transmission eigenchannels. We find that the other sources of incomplete control have relatively minor effects. In Fig. 5b we include the phase-only modulation of the incident wavefront, as well as the finite ranges of incident and collecting angles, which are set by the experimental NA in illumination and detection (see Supplementary Section 2.7 for details). The ranges of transmittance and the width of the eigenchannels both decrease, but the qualitative trends remain the same.

Finally, we also model the effect of experimental noise (see Supplementary Section 2.7 for details). As shown in Fig. 5c, the low-transmission eigenchannels are more sensitive to noise than the high-transmission channels: the input widths of low-transmission channels approach those of random incident wavefronts, while the input widths of the high-transmission channels only change slightly. The transverse spreads ΔD of all eigenchannels are plotted in Supplementary Fig. 10. These results agree qualitatively with our experimental data.

Conclusion

In summary, we have discovered transverse localization of transmission eigenchannels in diffusive slabs. In the presence of complete control, each eigenchannel has statistically identical input and output widths as a result of optical reciprocity. In a 2D slab, the asymptotic width for open channels is $D_\infty \approx (2/3)kl_tL$, due to the bandedness and non-local correlations of the real-space transmission matrix. Experimentally, with a finite illumination area, we observe signatures of transverse localization including enhanced lateral confinement, suppressed spreading and exponentially decaying tails for high-transmission channels. The transverse localization results from wave interference effects, which are enhanced by non-local correlations. Due to the reduced illumination area and suppressed lateral spreading, a high-transmission channel is confined into a volume significantly smaller than that from a random wavefront, leading to a significant enhancement of optical energy density that is important for light–matter interactions, imaging and optogenetics in scattering media.

Online content

Any methods, additional references, Nature Research reporting summaries, source data, statements of data availability and associated accession codes are available at https://doi.org/10.1038/s41566-019-0367-9.

Received: 4 June 2018; Accepted: 23 January 2019;
Published online: 4 March 2019

References

1. Dorokhov, O. N. On the coexistence of localized and extended electronic states in the metallic phase. *Solid State Commun.* **51**, 381–384 (1984).
2. Imry, Y. Active transmission channels and universal conductance fluctuations. *Europhys. Lett.* **1**, 249–256 (1986).
3. Mello, P. A., Pereyra, P. & Kumar, N. Macroscopic approach to multichannel disordered conductors. *Ann. Phys.* **181**, 290–317 (1988).
4. Nazarov, Y. V. Limits of universality in disordered conductors. *Phys. Rev. Lett.* **73**, 134–137 (1994).
5. Mosk, A. P., Lagendijk, A., Lerosey, G. & Fink, M. Controlling waves in space and time for imaging and focusing in complex media. *Nat. Photon.* **6**, 283–292 (2012).
6. Vellekoop, I. M. Feedback-based wavefront shaping. *Opt. Express* **23**, 12189–12206 (2015).
7. Rotter, S. & Gigan, S. Light fields in complex media: mesoscopic scattering meets wave control. *Rev. Mod. Phys.* **89**, 015005 (2017).
8. Vellekoop, I. M. & Mosk, A. P. Universal optimal transmission of light through disordered materials. *Phys. Rev. Lett.* **101**, 120601 (2008).
9. Kim, M. et al. Maximal energy transport through disordered media with the implementation of transmission eigenchannels. *Nat. Photon.* **6**, 581–585 (2012).
10. Kim, M., Choi, W., Yoon, C., Kim, G. H. & Choi, W. Relation between transmission eigenchannels and single-channel optimizing modes in a disordered medium. *Opt. Lett.* **38**, 2994–2996 (2013).
11. Popoff, S. M., Goetschy, A., Liew, S. F., Stone, A. D. & Cao, H. Coherent control of total transmission of light through disordered media. *Phys. Rev. Lett.* **112**, 133903 (2014).
12. Bosch, J., Goorden, S. A. & Mosk, A. P. Frequency width of open channels in multiple scattering media. *Opt. Express* **24**, 26472–26478 (2016).
13. Hsu, C. W., Liew, S. F., Goetschy, A., Cao, H. & Stone, A. D. Correlation-enhanced control of wave focusing in disordered media. *Nat. Phys.* **13**, 497–502 (2017).
14. Sarma, R., Yamilov, A. G., Petrenko, S., Bromberg, Y. & Cao, H. Control of energy density inside a disordered medium by coupling to open or closed channels. *Phys. Rev. Lett.* **117**, 086803 (2016).
15. Choi, W., Mosk, A. P., Park, Q.-H. & Choi, W. Transmission eigenchannels in a disordered medium. *Phys. Rev. B* **83**, 134207 (2011).
16. Gérardin, B., Laurent, J., Derode, A., Prada, C. & Aubry, A. Full transmission and reflection of waves propagating through a maze of disorder. *Phys. Rev. Lett.* **113**, 173901 (2014).
17. Davy, M., Shi, Z., Park, J., Tian, C. & Genack, A. Z. Universal structure of transmission eigenchannels inside opaque media. *Nat. Commun.* **6**, 6893 (2015).
18. Ojambati, O. S., Yılmaz, H., Lagendijk, A., Mosk, A. P. & Vos, W. L. Coupling of energy into the fundamental diffusion mode of a complex nanophotonic medium. *New J. Phys.* **18**, 043032 (2016).
19. Koirala, M., Sarma, R., Cao, H. & Yamilov, A. Inverse design of perfectly transmitting eigenchannels in scattering media. *Phys. Rev. B* **96**, 054209 (2017).
20. Hong, P., Ojambati, O. S., Lagendijk, A., Mosk, A. P. & Vos, W. L. Three-dimensional spatially resolved optical energy density enhanced by wavefront shaping. *Optica* **5**, 844–849 (2018).
21. Pendry, J. B. Quasi-extended electron states in strongly disordered systems. *J. Phys. C* **20**, 733 (1987).
22. Bertolotti, J., Gottardo, S., Wiersma, D. S., Ghulinyan, M. & Pavesi, L. Optical necklace states in Anderson localized 1D systems. *Phys. Rev. Lett.* **94**, 113903 (2005).
23. Sebbah, P., Hu, B., Klosner, J. M. & Genack, A. Z. Extended quasimodes within nominally localized random waveguides. *Phys. Rev. Lett.* **96**, 183902 (2006).
24. Choi, W., Park, Q.-H. & Choi, W. Perfect transmission through Anderson localized systems mediated by a cluster of localized modes. *Opt. Express* **20**, 20721–20729 (2012).
25. Peña, A., Girschik, A., Libisch, F., Rotter, S. & Chabanov, A. A. The single-channel regime of transport through random media. *Nat. Commun.* **5**, 3488 (2014).
26. Leseur, O., Pierrat, R., Sáenz, J. J. & Carminati, R. Probing two-dimensional Anderson localization without statistics. *Phys. Rev. A* **90**, 053827 (2014).
27. Skipetrov, S. E. & Page, J. H. Red light for Anderson localization. *New J. Phys.* **18**, 021001 (2016).
28. De Raedt, H., Lagendijk, A. & de Vries, P. Transverse localization of light. *Phys. Rev. Lett.* **62**, 47–50 (1989).
29. Schwartz, T., Bartal, G., Fishman, S. & Segev, M. Transport and Anderson localization in disordered two-dimensional photonic lattices. *Nature* **446**, 52–55 (2007).
30. Karbasi, S. et al. Observation of transverse Anderson localization in an optical fiber. *Opt. Lett.* **37**, 2304–2306 (2012).
31. Hsieh, P. et al. Photon transport enhanced by transverse Anderson localization in disordered superlattices. *Nat. Phys.* **11**, 268–274 (2015).
32. Hu, H., Strybulevych, A., Page, J. H., Skipetrov, S. E. & Van Tiggelen, B. A. Localization of ultrasound in a three-dimensional elastic network. *Nat. Phys.* **4**, 945–948 (2008).
33. Cherroret, N., Skipetrov, S. E. & Van Tiggelen, B. A. Transverse confinement of waves in three-dimensional random media. *Phys. Rev. E* **82**, 056603 (2010).
34. Horstmeyer, R., Ruan, H. & Yang, C. Guidestar-assisted wavefront-shaping methods for focusing light into biological tissue. *Nat. Photon.* **9**, 563–571 (2015).
35. Kim, M., Choi, W., Choi, Y., Yoon, C. & Choi, W. Transmission matrix of a scattering medium and its applications in biophotonics. *Opt. Express* **23**, 12648–12668 (2015).
36. Yu, H. et al. Recent advances in wavefront shaping techniques for biomedical applications. *Curr. Appl. Phys.* **15**, 632–641 (2015).
37. Vynck, K., Burresi, M., Riboli, F. & Wiersma, D. S. Photon management in two-dimensional disordered media. *Nat. Mater.* **11**, 1017–1022 (2012).
38. Liew, S. F. et al. Coherent control of photocurrent in a strongly scattering photoelectrochemical system. *ACS Photon.* **3**, 449–455 (2016).
39. Baranger, H. U., DiVincenzo, D. P., Jalabert, R. A. & Stone, A. D. Classical and quantum ballistic-transport anomalies in microjunctions. *Phys. Rev. B* **44**, 10637–10675 (1991).
40. Jalas, D. et al. What is—and what is not—an optical isolator. *Nat. Photon.* **7**, 579–582 (2013).
41. Freund, I., Rosenbluh, M. & Feng, S. Memory effects in propagation of optical waves through disordered media. *Phys. Rev. Lett.* **61**, 2328–2331 (1988).
42. Berkovits, R., Kaveh, M. & Feng, S. Memory effect of waves in disordered systems: a real-space approach. *Phys. Rev. B* **40**, 737–740 (1989).
43. Judkewitz, B., Horstmeyer, R., Vellekoop, I. M., Papadopoulos, I. N. & Yang, C. Translation correlations in anisotropically scattering media. *Nat. Phys.* **11**, 684–689 (2015).
44. Osnabrugge, G., Horstmeyer, R., Papadopoulos, I. N., Judkewitz, B. & Vellekoop, I. M. Generalized optical memory effect. *Optica* **4**, 886–892 (2017).
45. Casati, G., Molinari, L. & Izrailev, F. Scaling properties of band random matrices. *Phys. Rev. Lett.* **64**, 1851–1854 (1990).
46. Izrailev, F. M. Simple models of quantum chaos: spectrum and eigenfunctions. *Phys. Rep.* **196**, 299–392 (1990).
47. Fyodorov, Y. V. & Mirlin, A. D. Analytical derivation of the scaling law for the inverse participation ratio in quasi-one-dimensional disordered systems. *Phys. Rev. Lett.* **69**, 1093–1096 (1992).
48. Stephen, M. J. & Cwilich, G. Intensity correlation functions and fluctuations in light scattered from a random medium. *Phys. Rev. Lett.* **59**, 285–287 (1987).
49. Feng, S., Kane, C., Lee, P. A. & Stone, A. D. Correlations and fluctuations of coherent wave transmission through disordered media. *Phys. Rev. Lett.* **61**, 834–837 (1988).

50. Mello, P. A., Akkermans, E. & Shapiro, B. Macroscopic approach to correlations in the electronic transmission and reflection from disordered conductors. *Phys. Rev. Lett.* **61**, 459–462 (1988).
51. Pnini, R. & Shapiro, B. Fluctuations in transmission of waves through disordered slabs. *Phys. Rev. B* **39**, 6986–6994 (1989).
52. Berkovits, R. & Feng, S. Correlations in coherent multiple scattering. *Phys. Rep.* **238**, 135–172 (1994).
53. Genack, A. Z., Garcia, N. & Polkosnik, W. Long-range intensity correlation in random media. *Phys. Rev. Lett.* **65**, 2129–2132 (1990).
54. Scheffold, F., Härtl, W., Maret, G. & Matijevíc, E. Observation of long-range correlations in temporal intensity fluctuations of light. *Phys. Rev. B* **56**, 10942–10952 (1997).
55. Sebbah, P., Hu, B., Genack, A. Z., Pnini, R. & Shapiro, B. Spatial-field correlation: the building block of mesoscopic fluctuations. *Phys. Rev. Lett.* **88**, 123901 (2002).
56. Yamilov, A. Relation between channel and spatial mesoscopic correlations in volume-disordered waveguides. *Phys. Rev. B* **78**, 045104 (2008).
57. Strudley, T., Zehender, T., Blejean, C., Bakkers, E. P. A. M. & Muskens, O. Mesoscopic light transport by very strong collective multiple scattering in nanowire mats. *Nat. Photon.* **7**, 413–418 (2013).
58. Fayard, N., Cazé, A., Pierrat, R. & Carminati, R. Intensity correlations between reflected and transmitted speckle patterns. *Phys. Rev. A* **92**, 033827 (2015).
59. Starshynov, I. et al. Non-Gaussian correlations between reflected and transmitted intensity patterns emerging from opaque disordered media. *Phys. Rev. X* **8**, 021041 (2018).
60. Akkermans, E. & Montambaux, G. *Mesoscopic Physics of Electrons and Photons* (Cambridge Univ. Press, Cambridge, 2007).
61. Popoff, S. M. et al. Measuring the transmission matrix in optics: an approach to the study and control of light propagation in disordered media. *Phys. Rev. Lett.* **104**, 100601 (2010).
62. Sheng, P. *Introduction to Wave Scattering, Localization and Mesoscopic Phenomena* (Academic Press, San Diego, CA, 1995).
63. Kramer, B. & MacKinnon, A. Localization: theory and experiment. *Rep. Prog. Phys.* **56**, 1469–1564 (1993).
64. Goetschy, A. & Stone, A. D. Filtering random matrices: the effect of incomplete channel control in multiple scattering. *Phys. Rev. Lett.* **111**, 063901 (2013).

Acknowledgements

We thank A. Mosk, A. Genack, B. Shapiro, F. Scheffold, S. Skipetrov, S. Bittner, S. Rotter and T. Kottos for stimulating discussions and useful feedback. We acknowledge financial support by the Office of Naval Research (ONR) under grant no. MURI N00014-13-0649 and by the US–Israel Binational Science Foundation (BSF) under grant no. 2015509, as well as computational resources provided by the Yale High Performance Computing Cluster (Yale HPC).

Author contributions

H.Y. performed the experiments and analysed the data. C.W.H. performed the numerical simulations and fabricated the samples. H.Y. analysed the numerical data. C.W.H. helped with experimental data acquisition and contributed to numerical data analysis. H.C. supervised the project. All authors contributed to the interpretation of the results. H.Y. and C.W.H. prepared the manuscript, H.C. edited it and A.Y. provided feedback.

Competing interests

The authors declare no competing interests.

Additional information

Supplementary information is available for this paper at https://doi.org/10.1038/s41566-019-0367-9.

Reprints and permissions information is available at www.nature.com/reprints.

Correspondence and requests for materials should be addressed to H.C.

Publisher's note: Springer Nature remains neutral with regard to jurisdictional claims in published maps and institutional affiliations.

Methods

Numerical simulation of transmission eigenchannels. We solve the 2D scalar wave equation $[\nabla^2 + k_0^2\epsilon(\mathbf{r})]\psi(\mathbf{r}) = 0$ on a finite-difference grid, where k_0 is the vacuum wavenumber, $\epsilon(\mathbf{r})$ the dielectric constant at spatial position $\mathbf{r}$, and $\psi(\mathbf{r})$ the electric field at $\mathbf{r}$. We consider disordered slabs of width W and thickness L in background refractive index n_0. The dielectric constant of the slab is modelled as $\epsilon(\mathbf{r}) = n_0^2 + \delta\epsilon(\mathbf{r})$ at each grid point, and $\delta\epsilon(\mathbf{r})$ is a random number drawn from a zero-mean uniform distribution whose width determines the transport mean free paths l_t (see Supplementary Section 2.1 for details). After calculating the field transmission matrix t for the entire slab using the recursive Green's function method[39], we obtain the incident wavefront V_n of an eigenchannel via $t^\dagger t V_n = \tau_n V_n$, and calculate its spatial profile with such an incident wavefront. In this work we focus on scattering systems in the diffusive regime of transport, namely $Nl_t \gg L \gg l_t$, where $N \approx kW/\pi$ is the number of modes.

Participation number. The lateral width of an eigenchannel is given by the participation number of its transverse intensity profile. The input width is found from the expression

$$D_{\rm in} \equiv \frac{\left[\int_0^W |V_n(x)|^2\, {\rm d}x\right]^2}{\int_0^W |V_n(x)|^4\, {\rm d}x}$$

where $V_n(x)$ is the incident field distribution at the input surface obtained from the nth eigenvector of $t^\dagger t$. Similarly, the output width $D_{\rm out}$ of the nth eigenchannel is obtained from the transmitted field distribution $U_n(x)$ at the output surface. For a 2D intensity distribution $I(x,y)$, its effective area A is computed from the 2D participation number:

$$A \equiv \frac{\left[\iint I(x,y){\rm d}x{\rm d}y\right]^2}{\iint I^2(x,y){\rm d}x{\rm d}y}$$

Data availability

The data that support the plots within this paper and other findings of this study are available from the corresponding author upon reasonable request.